



저작자표시-비영리-동일조건변경허락 2.0 대한민국

이용자는 아래의 조건을 따르는 경우에 한하여 자유롭게

- 이 저작물을 복제, 배포, 전송, 전시, 공연 및 방송할 수 있습니다.
- 이차적 저작물을 작성할 수 있습니다.

다음과 같은 조건을 따라야 합니다:



저작자표시. 귀하는 원저작자를 표시하여야 합니다.



비영리. 귀하는 이 저작물을 영리 목적으로 이용할 수 없습니다.



동일조건변경허락. 귀하가 이 저작물을 개작, 변형 또는 가공했을 경우에는, 이 저작물과 동일한 이용허락조건하에서만 배포할 수 있습니다.

- 귀하는, 이 저작물의 재이용이나 배포의 경우, 이 저작물에 적용된 이용허락조건을 명확하게 나타내어야 합니다.
- 저작권자로부터 별도의 허가를 받으면 이러한 조건들은 적용되지 않습니다.

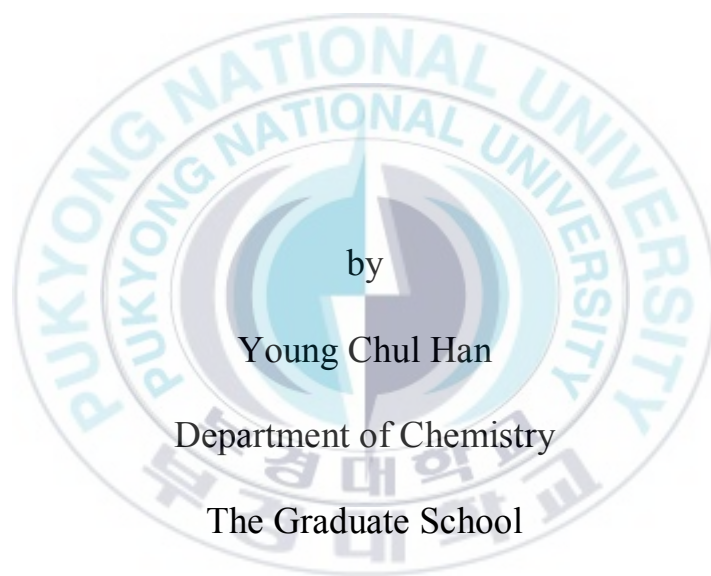
저작권법에 따른 이용자의 권리는 위의 내용에 의하여 영향을 받지 않습니다.

이것은 [이용허락규약\(Legal Code\)](#)을 이해하기 쉽게 요약한 것입니다.

[Disclaimer](#)

Thesis for the Degree of Master of Science

Study on the Preparation of Highly
Magnetized Magnetic Nanoparticles
and Effect of γ -Ray Irradiation on
Permanent Magnet



by

Young Chul Han

Department of Chemistry

The Graduate School

Pukyong National University

February 2008

Study on the Preparation of Highly
Magnetized Magnetic Nanoparticles
and Effect of γ -Ray Irradiation on
Permanent Magnet

(강자성 나노입자의 제조와
영구자석에 대한 감마선의 영향)

Advisor : Prof. Young Soo Kang

by

Young Chul Han

A thesis submitted in partial fulfillment of the requirements
for the degree of

Master of Science

in Department of Chemistry, The Graduate School,
Pukyong National University

February 2008

Study on the Preparation of Highly Magnetized
Magnetic Nanoparticles
and Effect of γ -Ray Irradiation on
Permanent Magnet

A dissertation
by
Young Chul Han

Approved by:

(Chairman)

(Member)

(Member)

(Member)

(Member)

November 2008

Study on the Preparation of Highly Magnetized Magnetic Nanoparticles and Effect of γ -Ray Irradiation on Permanent Magnet

Young Chul Han

Research Advisor: Prof. Young Soo Kang

*Department of Chemistry, The Graduated School, Pukyong National
University*

Abstract

In this research, the highly magnetized α -Fe nanoparticle was synthesized by the solventless thermal decomposition method. And, the effect of γ -ray irradiation on permanent magnet was also investigated. The solventless thermal decomposition method by capping agents is useful for the synthesis of pure metal nanoparticles. However the magnetic nanomaterials by the thermal decomposition method can not generally exhibit high magnetic properties like that of bulk magnetic material due to the existence of the surfactant and its pinning phenomenon. The high magnetic properties can be obtained by reduction in the high temperature with high vacuum and the NaCl powder which was used instead of a surfactant can be important separating media to keep the size and shape of nanoparticles. Other study is the investigation of the effect of ^{60}Co γ -ray irradiation on the microstructure of Nd-Fe-B permanent magnets at low temperature and

room temperature. Like other strong electromagnetic radiation source, the γ -ray has enough energy to the ionization of molecules, stripping electrons, and breaking of the chemical chain. When the magnets are exposed on γ -ray irradiation, they showed the reduced magnetism. The curie temperature, electronic structure, surface morphology of magnet were also changed.



Contents

ABSTRACT	i
LIST OF FIGURES.....	v
PART I. Synthesis of Highly Magnetized Iron Nanoparticle	
I. Introduction.....	1
II. Theory.....	3
III. Experimental.....	4
3.1. Materials.....	4
3.2. Synthesis of Fe ₃ O ₄ Nanoparticles.....	5
3.3. Synthesis of α -Fe Nanoparticles.....	5
3.4. Characterization.....	7
IV. Results and Discussion.....	8
4.1. Thermal properties of nanoparticles.....	8
4.2. Crystal structure of nanoparticles.....	10
4.3. Size and shape of nanoparticles.....	12
4.4. Decomposition of oleate.....	15
4.5. Magnetic property of nanoparticles.....	17
V. Conclusion.....	19
VI. References.....	20
PART II. Investigation of the Effect of γ-Ray Irradiation on the Permanent Magnets	
I. Introduction.....	22
II. Theory.....	23
III. Experimental	24
3.1. Materials.....	24
3.2. Preparing the Nd-Fe-B powder.....	25
3.3. γ -ray irradiation.....	27
3.4. Characterization.....	27

IV. Results and Discussion.....	29
4.1. Magnetic properties.....	29
4.2. Ordering energy of domain.....	32
4.3. Change of electronic structure.....	33
4.4. Crystal structure of Nd-Fe-B and Sr-Ferrite powder.....	37
4.5. Morphology of Nd-Fe-B and Sr-Ferrite powder.....	40
V. Conclusion.....	43
VI. References.....	46
KOREAN ABSTRACT.....	49



List of Figures

Figure 1.1. Overall scheme for a modified thermal decomposition method of α -Fe nanoparticle synthesis.....	4
Figure 1.2. The synthetic process of α -Fe nanoparticle.....	7
Figure 1.3. TGA curves of prepared Fe^{2+} -oleate ₂ complexes (a) and Fe_3O_4 nanoparticles (b).....	10
Figure 1.4. XRD diffraction patterns of prepared Fe_3O_4 (a) and α -Fe nanoparticles (b).....	12
Figure 1.5. TEM image (a), histogram of the size distribution (b) of Fe_3O_4 nanoparticles.....	14
Figure 1.6. TEM image (a) and histogram of size distribution (b) of α -Fe nanoparticles.....	14
Figure 1.7. HR-TEM image (a and b) of α -Fe nanoparticles annealed with NaCl powder under high vacuum system.....	15
Figure 1.8. EDX spectrum of Fe_3O_4 nanoparticles.....	16
Figure 1.9. TGA curve of α -Fe nanoparticles annealed with NaCl powder under high vacuum system.....	16
Figure 1.10. EPMA data of α -Fe nanoparticles annealed with NaCl powder under high vacuum system.....	17
Figure 1.11. VSM curves of prepared nanoparticles: (a) prepared Fe_3O_4 nanoparticles and (b) α -Fe nanoparticles annealed with NaCl powder under high vacuum.....	18
Figure 2.1. The preparing process of Nd-Fe-B particle.....	26
Figure 2.2. Scheme for a Hall probe to measure the magnetic field of samples.....	29
Figure 2.3. The magnetic field change of sintered $\text{Nd}_2\text{Fe}_{14}\text{B}$ magnets having different sizes $10\Phi \times 15 \text{ mm}^3$ (a,b), $10\Phi \times 10 \text{ mm}^3$ (c,d), $10\Phi \times 5 \text{ mm}^3$ (e,f), and $5 \times 5 \times 1 \text{ mm}^3$ (g,h) versus doses of ^{60}Co γ - r a y i r r a d i a t i o n a n d temperature.....	31
Figure 2.4. VSM curves of ball milled $\text{Nd}_{15}\text{Fe}_{77}\text{B}_8$ powders: as-heat treated and after γ -ray irradiated from 25 Mrad to 100 Mrad at room temperature of $26.5 \text{ }^\circ\text{C}$ and low temperature of $-78.5 \text{ }^\circ\text{C}$	31
Figure 2.5. VSM curves of $\text{SrFe}_{12}\text{O}_{19}$ powders: as-heat treated and	

after γ -ray irradiated from 25 Mrad to 100 Mrad at room temperature of 26.5 °C and low temperature of -78.5 °C.....	32
Figure 2.6. The TMA curves of Nd ₂ Fe ₁₄ B magnet before (a) and after 100 Mrad of ⁶⁰ Co γ -ray irradiation at low temperature (-78.5 °C, b) and room temperature (26.5 °C).....	33
Figure 2.7. The ESR spectra of Nd ₂ Fe ₁₄ B magnets before ⁶⁰ Co γ -ray irradiation (a) and after γ -ray irradiation at 25 Mrad (b), 50 Mrad (c), 75 Mrad (d), and 100 Mrad (e)	35
Figure 2.8. The EDX spectrum of Nd ₂ Fe ₁₄ B magnets.....	35
Figure 2.9. ESR spectra of the Nd ₂ Fe ₁₄ B magnet before γ -ray irradiation with different microwave power.....	36
Figure 2.10. ESR spectra with different microwave power of the Nd ₂ Fe ₁₄ B magnet after γ -ray irradiation at 100 Mrad.....	36
Figure 2.11. Progressive saturation of the Nd ₂ Fe ₁₄ B magnet before (a) and after γ -ray irradiation at 100 Mrad (b) by ESR spectra with different microwave power.....	37
Figure 2.12. XRD pattern of ball milled Nd ₁₅ Fe ₇₇ B ₈ powders: as-heat treated (a), after γ -ray irradiated of 25 Mrad at 26.5 °C (b), 25 Mrad at -78.5 °C (c), 100 Mrad at 26.5 °C (d), 100 Mrad at -78.5 °C (e).....	39
Figure 2.13. XRD pattern of SrFe ₁₂ O ₁₉ powder: before γ -ray irradiated (a), after γ -ray irradiated of 25 Mrad at 26.5 °C (b), 25 Mrad at -78.5 °C (c), 100 Mrad at 26.5 °C (d), 100 Mrad at -78.5 °C (e).....	39
Figure 2.14. SEM images of ball milled Nd ₂ Fe ₁₄ B powders: as-heat treated (a), after γ -ray irradiated of 25 Mrad at 26.5 °C (b), 25 Mrad at -78.5 °C (c), 100 Mrad at 26.5 °C (d), 100 Mrad at -78.5 °C (e)	41
Figure 2.15. SEM images of SrFe ₁₂ O ₁₉ : before γ -ray irradiated (a), after γ -ray irradiated of 25 Mrad at 26.5 °C (b), 25 Mrad at -78.5 °C (c), 100 Mrad at 26.5 °C (d), 100 Mrad at -78.5 °C (e).....	42

List of Tables

Table 1.1: Angle (θ) and FWHM of XRD spectra for Fe_3O_4 and α -Fe nanoparticles.....	12
Table 1.2: Magnetic properties of prepared Fe_3O_4 and α -Fe nanoparticles.....	19
Table 2.1: Magnetic values of $\text{Nd}_2\text{Fe}_{14}\text{B}$ based magnet (N30H) used in this study.....	25



Part I.

Synthesis of Highly Magnetized Iron Nanoparticle

1. Introduction

Particular inorganic nanoparticles have been extensively studied during this decade because of their real or expected physical properties resulting from their nanosize and special application.^{1,2} The interest in the properties of these objects has evidenced the need for the control of monodispersity, size, shape, organization, and nature of the chemical species presented at their surface.^{3,4} In magnetic nanomaterials, the development of size-controlled nanoparticles became a very important issue in their application to permanent magnets with high performance,^{5,6} the targeted delivery of drugs,⁷ and the ultrahigh density magnetic storage device.⁸ One of the most representative magnetic materials for the application is metal oxides such as various ferrites, and these ferrite magnetic materials were significantly studied by Hyeon . for their chemical stability, uniform size, and shape.⁹ α -Fe is also of particular interest for the previously mentioned applications as compared with currently used maghemeite (γ -Fe₂O₃) and magnetite (Fe₃O₄) because its higher magnetic properties can lead to improved magnetic performance in various fields.¹⁰⁻¹²

As a matter of fact, one of many problems for the synthesis of magnetic nanoparticles is that the particles easily aggregate to each other owing to their magnetism and van der Waals attraction. The particle aggregation can be caused by unwanted particle growth during the synthetic and annealing process. In addition, there are other problems associated with the oxidation of metallic nanoparticles. In the case of the thermal decomposition method, the magnetic nanomaterials cannot generally exhibit high magnetic properties like those of bulk magnetic material due to the existence of the surfactant and its pinning phenomenon of the surface spins by surfactants coated on the surface of the magnetic nanoparticle.¹³ Moreover, after just annealing the nanoparticle at a high temperature, it is difficult for the magnetic decline to be overcome. Rather, it causes a dissatisfied morphology because of particle growth by the increased thermal effect.

The solventless thermal decomposition method by capping agents such as oleate can be used for the synthesis of pure metal nanoparticles in regulated conditions either spontaneously or in the presence of a reducing gas. Moreover, it is free of environmental pollution by the toxic solvent. This is a valuable alternative to solve these problems for the synthesis of nanosized materials.¹⁴⁻¹⁷ If surfactants coated on the nanoparticles using the separating media are removed from the surface of the nanoparticles as much as possible, better magnetic properties and adequate morphology will be obtained comparable to that of conventional techniques. Elkins *et al.* reported excellent work about the transformation of FePt nanoparticles from a fcc crystal structure to a fct structure with mashed salt powder that

was used as a separating media between FePt nanoparticles, and in this work, the phase of the FePt nanoparticles was successfully transformed without aggregation.¹⁸

In our work, because of the utility factor that is easily soluble in water with a high stability at high temperatures (melting point is 801 °C) and economical merits, NaCl powder was used as a separating media or surfactant. The α -Fe nanoparticles having a saturation magnetization value of 213 emu/g were synthesized by the reduction of Fe₃O₄ nanoparticles using NaCl powder under a high vacuum system at 1.8×10^{-5} Torr. The solventless thermal decomposition method with NaCl powder instead of a surfactant on the surface of the nanoparticles can be a valuable alternative to suppress the increase of the particle size.

2. Theory

The overall synthetic procedure is depicted in Figure 1.1, and the detailed experimental procedures are described in the previous section. First, the Fe²⁺-oleate₂ complex was synthesized using iron (II) chloride tetrahydrate and sodium oleate. Sodium oleate was used as a capping agent because oleate has a C₁₈ (oleic) tail with a cis double bond in the middle, forming a kink. Such kinks have been postulated as necessary for effective stabilization, and indeed, stearic acid (CH₃(CH₂)₁₆-COOH) with no double bond in its C₁₈ tail cannot stabilize suspensions.¹⁹ Fe₃O₄ nanoparticles were obtained by solventless thermal decomposition using the pyrex tube from the synthesized Fe²⁺-oleate₂ complexes. The prepared Fe₃O₄ nanoparticles

were mixed with NaCl powder by a shaker miller to be as uniform as possible. Through the NaCl powder as separating media, each Fe₃O₄ nanoparticle was separated during the course of reduction by H₂ gas and annealing under a high vacuum system of 1.8×10^{-5} torr to obtain a high saturation magnetization value of α -Fe nanoparticles. If the ratio between NaCl and Fe₃O₄ nanoparticles is lower than 1:40, the effect of keeping the size and shape during the reduction and annealing of the NaCl powder for the separating media was decreased. However, when the ratio is higher than 1:40, it is difficult to deal with the mixture powder for washing and annealing.¹⁸

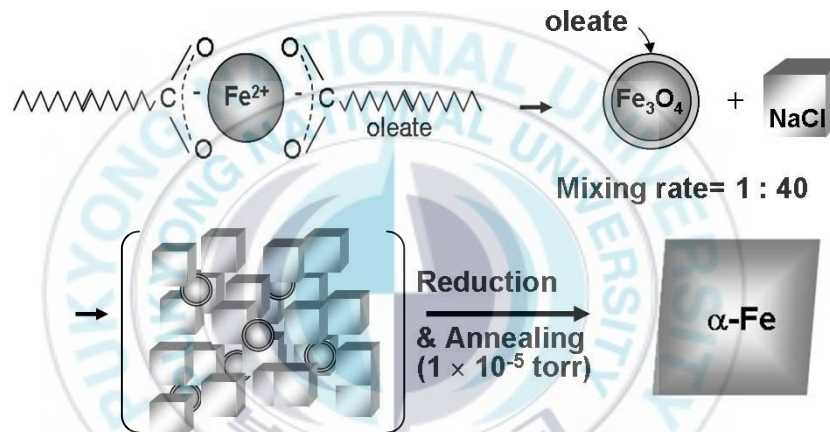


Figure 1.1 Overall scheme for a modified thermal decomposition method of α -Fe nanoparticle synthesis.

3. Experimental

3.1. Materials

The experiments were carried out by using an Fe^{2+} -oleate₂ complex prepared from iron (II) chloride tetrahydrate ($\text{FeCl}_2 \cdot 4\text{H}_2\text{O}$, 99+%), and sodium oleate ($\text{C}_{17}\text{H}_{33}\text{COONa}$, 98%). The compounds were purchased from Aldrich and used without further purification. High purity Ar gas (99.999+%) was used for purging the distilled water (18 M Ω) and to prevent the oxidation of the prepared nanoparticles. To refine the as annealed Fe_3O_4 and α -Fe, chloroform (99.5%), methanol (99.75%), and acetone (99.5%) from Junsei Chemical Co. were used. An Ar mixture gas (+4% H_2) and sodium chloride powder (99.5%, Shinyo Pure Chemical Co.) were used to reduce the Fe_3O_4 nanoparticles.

3.2. Synthesis of Fe_3O_4 Nanoparticles

The Fe^{2+} -oleate₂ complex was prepared from iron (II) chloride tetrahydrate and sodium oleate. A total of 2.0 g of iron (II) chloride tetrahydrate (10 mmol) and 6.09 g of sodium oleate (20 mmol) were dissolved in deoxygenated water of 100 mL and 200 mL each using a magnetic stirrer. The resulting iron salt solution was slowly added into the sodium oleate solution at a dropping rate of 0.5 mL/s. When the white Fe^{2+} -oleate₂ complexes were precipitated enough, they were separated by filtering and washed with deoxygenated water to be free of sodium and chloride ions. Then, the as-filtrated Fe^{2+} -oleate₂ complexes were dried in a glovebox with Ar gas. Dried complexes were transferred to pyrex tube and sealed at 2.4×10^{-2} torr. The tube was heated from room temperature to 400 °C at 1 °C/min.²⁰ The dried Fe^{2+} -oleate₂ complexes in the pyrex tube were kept at 400 °C for 2 hrs and then is was cooled to room temperature. The thermally

decomposed oleates during nucleation and growth of Fe_3O_4 nanoparticles by the pyrex tube at $400\text{ }^\circ\text{C}$ were washed by centrifuging with ethanol and chloroform in a volume ratio of 5:1 (ethanol/chloroform). In this course, most of the decomposed oleates except partial oleates on the surface of Fe_3O_4 nanoparticles were removed.

3.3. Synthesis of α -Fe Nanoparticles

As-made Fe_3O_4 nanoparticles were mixed with NaCl powders that were then dried in the furnace and mashed by ball milling for more than 24 hrs. Then, the mixtures were ball-milled for 24 hrs in a ratio of 1:40 (wt of Fe_3O_4 /wt of NaCl).¹⁹ The ball-milled powder was reduced at $700\text{ }^\circ\text{C}$ for 30 min under $\text{Ar} + 4\% \text{H}_2$ gas, and it was re-annealed under the vacuum system at 1.8×10^{-5} torr at $700\text{ }^\circ\text{C}$ for 3 hrs.^{15,21} As-annealed powder was washed with deoxygenated water and acetone to remove the used NaCl powder and deoxygenated water. The Ar-dried α -Fe nanoparticles were stored in cyclohexane to keep from oxidizing. The process was performed in a glovebox under a high purity Ar atmosphere. Figure 1.2 shows the synthetic process of α -Fe nanoparticles.

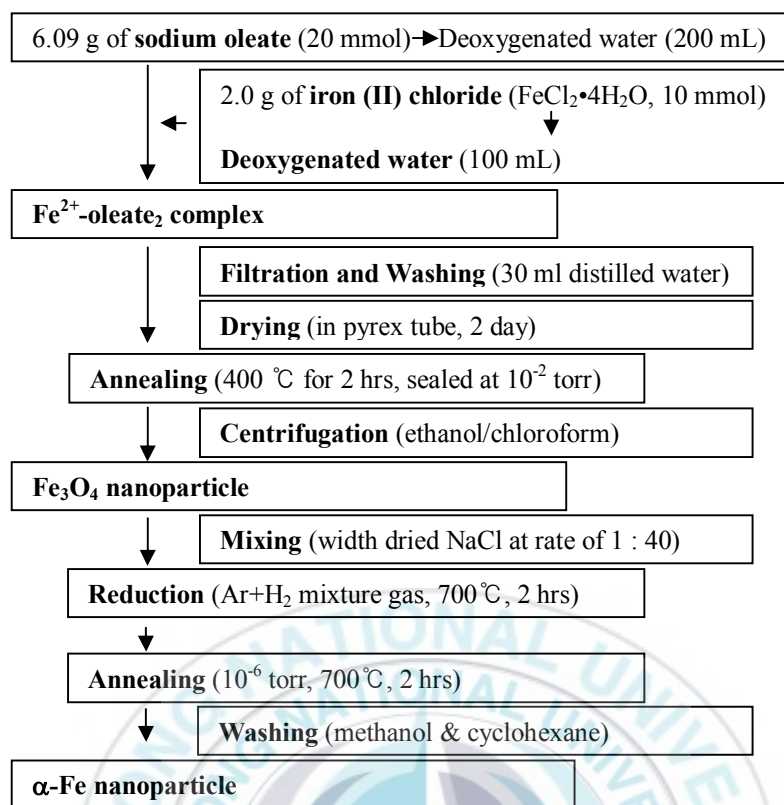


Figure 1.2 The synthetic process of α -Fe nanoparticle.

3.4. Characterization

To identify the structure and properties of the prepared α -Fe nanoparticles, we performed various experiments. The thermal property of the as-synthesized Fe^{2+} -oleate₂ complexes and prepared nanoparticles was analyzed by thermogravimetric analysis (TGA), which was collected at a heating rate of 10 °C/min with the sample kept under a high purity argon atmosphere. The crystal structure and mean size of the prepared nanoparticles were investigated using X-ray powder diffraction (XRD) with a Philips X'pert-MPD System using a

monochromated Cu-K α radiation source ($\lambda=0.154056$ nm). Moreover, elemental analyses were conducted using an electron probe X-ray micro-analyzer (EPMA-1600, Shimadzu), and energy dispersive X-ray microanalysis (EDX) with a JEOL JEM2010 TEM system was operated under an acceleration voltage of 200 kV. To confirm the morphology of prepared nanoparticles, a transmission electron microscope (Hitachi-7500 TEM) was used. The size distribution of the nanoparticles was measured from enlarged photographs of TEM images. The magnetic properties such as saturation magnetization and coercivity were measured by a Lake Shore 7300 vibrating sample magnetometer (VSM) with an applied field up to 15 kOe after the powder sample was set with wax to prevent physical rotation of the particles.

4. Results and Discussion

4.1 Thermal properties of nanoparticles

Figure 1.3 shows TGA curves of Fe²⁺-oleate₂ complexes (spectrum a) and the obtained Fe₃O₄ nanoparticles (spectrum b). In the thermograms of the Fe²⁺-oleate₂ complexes, strong endothermic peaks were observed at 215.24, 344.26, and 448.64 °C. The actual mass loss amounted to 88.54 wt % during the interval. This indicates that the Fe ion is bound with oleate at a ratio of 1:2 and that it agrees with the configuration of the Fe²⁺-oleate₂ complex in Figure 1.1. When the Fe²⁺-oleate₂ complexes were heated at about 200 °C, weakly absorbed oleate dissociated in the complex, and the remaining oleate

directly absorbed on the surface of the Fe₃O₄ nanoparticles dissociated at about 300 °C and decomposed by a CO₂ elimination pathway.⁹ During this course, oxygen in CO₂ as well as H₂ were also eliminated from oleate.²² The formation of Fe₃O₄ nanoparticles was caused by the oxidation of Fe by decomposition of oleate during a heating process at 400 °C in the pyrex tube. The TGA curve of Fe₃O₄ nanoparticles shown in Figure 1.3 b indicates that the 60.26 wt % oleate coated on the surface of the Fe₃O₄ nanoparticles was removed at a temperature of 776.01 °C. These results indicate that most of the mass loss occurs around 450 and 750 °C and that the thermal decomposition of oleate occurred at these temperatures. The α-Fe nanoparticle was easily prepared by the reduction of Fe₃O₄ nanoparticles with annealing by H₂ gas over 600 °C, and the relative chemical equation can be written according to eq 1^{23,24}



The thermal reduction by the equation is useful to our work. At temperatures over 600 °C, H₂ is a strong reducer with a high chemical activity, and it could react with the O²⁻ ion easily.

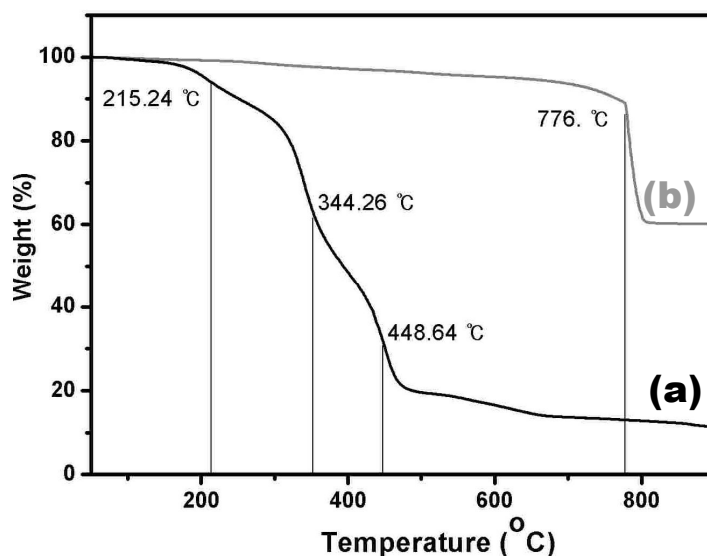


Figure 1.3. TGA curves of prepared Fe^{2+} -oleate₂ complexes (a) and Fe_3O_4 nanoparticles (b).

4.2. Crystal structure of nanoparticles

By the formation of a molecule such as H_2O , the O^{2-} ion in the Fe_3O_4 particles is adequately removed, and Fe_3O_4 nanoparticles are successfully transformed to α -Fe nanoparticles as the XRD pattern of the prepared Fe_3O_4 and α -Fe nanoparticles is shown in Figure 1.4. Discernible peaks of the XRD pattern are clearly seen in the Figure (a, and this corresponds to cubic Fe_3O_4 nanoparticles (JCPDS Card No. 03-0862), and peaks in Figure 1.4 b can be indexed to (110), (200), and (211) planes of the cubic unit cell. This corresponds to that of an α -Fe structure (JCPDS Card No. 06-0696). Diffraction peaks associated with NaCl or any other phases such as metal oxides were not found in the XRD patterns. This indicates a minimal contamination of the product by the salt during annealing. The

average diameter (D) of the particles can be calculated from the broadening of the respective high intensity XRD peak using the Scherrer equation²⁵

$$D = k\lambda/\beta \cos\theta$$

where k is the Scherrer factor (0.89), λ is the X-ray wavelength (here, $\lambda = 1.54178 \text{ \AA}$), β is the line broadening of a diffraction peak at angle θ , and β is measured using the following equation:

$$\beta = (B^2 - b_0^2)^{1/2}$$

where B is the measured FWHM of the experimental profile in degrees and b_0 is the instrumental broadening, which was obtained from the scans of standard silicon powder. The average diameter increased from 22.15 nm (spectrum a) to 35.57 nm (spectrum b) of the Fe_3O_4 nanoparticles, and $\alpha\text{-Fe}$ nanoparticles were calculated. The angle (θ) and FWHM of these XRD patterns are shown in Table 1.1.

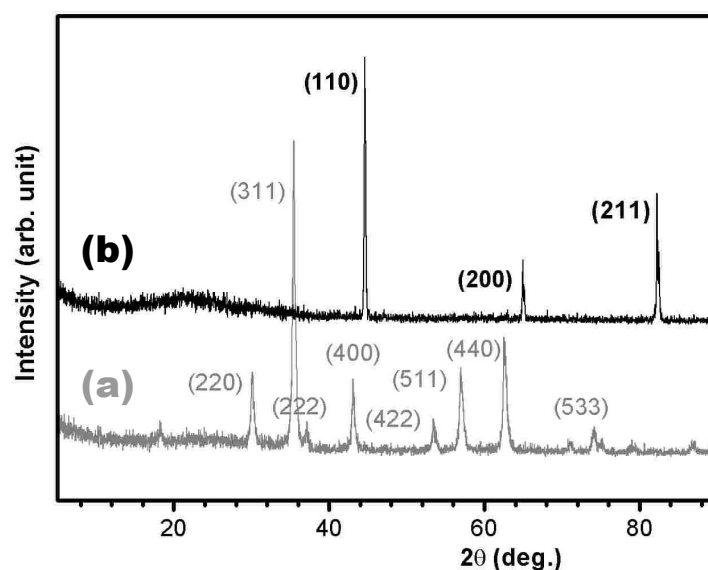


Figure 1.4. XRD diffraction patterns of prepared Fe_3O_4 (a) and $\alpha\text{-Fe}$ nanoparticles (b).

Table 1.1: Angle (θ) and FWHM of XRD spectra for Fe_3O_4 and $\alpha\text{-Fe}$ nanoparticles

	θ	FWHM	Av diameter
Fe_3O_4 nanoparticles (Figure 3a)	35.46	0.37	22.15 nm
$\alpha\text{-Fe}$ nanoparticles (Figure 3b)	44.48	0.23	35.57 nm

4.3. Size and shape of nanoparticles

Figure 1.5 shows the TEM image (panel a), the histogram of the size distribution (panel b) of Fe_3O_4 nanoparticles that were annealed in a pyrex tube at $400\text{ }^\circ\text{C}$ for 2 hrs. As can be seen in the TEM images, the size of the Fe_3O_4 nanoparticles was determined to be around $18 \sim 24\text{ nm}$ (panel b), and it shows a comparatively uniform shape. These values are close to the particle sizes that were calculated by the Debye-Scherrer equation with XRD data in Figure 1.4. Figure 1.6

shows the TEM image (panel a), the histogram of size distribution (panel b) of α -Fe nanoparticles annealed with NaCl powder under a high vacuum system. When the prepared Fe_3O_4 nanoparticles were reduced and annealed under a high vacuum at 700 °C for 3 hrs with NaCl powder, it was found that the annealed particles were easier to aggregate because of the magnetic attraction force between the α -Fe nanoparticles, and this aggregation can be re-dispersed in ethanol by ultrasonic vibration. The particle size of prepared α -Fe nanoparticles ranges from 18 to 42 nm with a mean diameter of about 36 nm. The morphology of the obtained α -Fe nanoparticles was not perfectly controlled, but it was confirmed that the annealing with NaCl powder under high vacuum can control the morphology. This is a good result as compared with the α -Fe nanoparticles prepared by reduction under an Ar + H₂ gas atmosphere at 800 °C for 3 hrs without NaCl. This also indicates that the NaCl powder can be used to suppress the deteriorating magnetic property and to maintain the same size and shape of the α -Fe particles as those prepared using a surfactant. Figure 1.7 shows the HR-TEM images of α -Fe nanoparticles annealed with NaCl powder under a high vacuum system. The lattice spacing (panels a and b) of the α -Fe nanocrystallite is 2.02 Å, which is consistent with the lattice spacing of the (110) plane of the α -Fe crystal structure (JCPDS Card No. 06-0696).

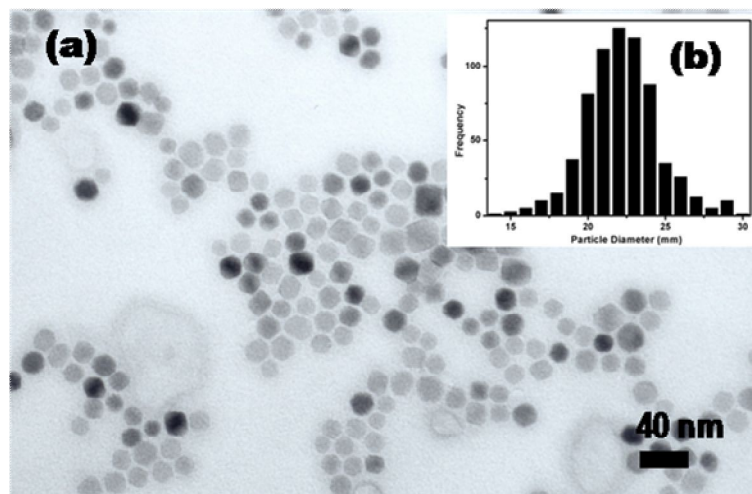


Figure 1.5. TEM image (a), histogram of the size distribution (b) of Fe_3O_4 nanoparticles.

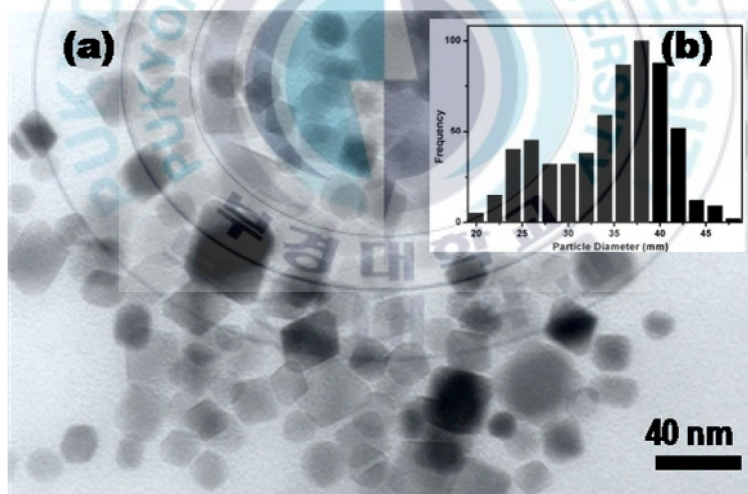


Figure 1.6. TEM image (a) and histogram of size distribution (b) of $\alpha\text{-Fe}$ nanoparticles.

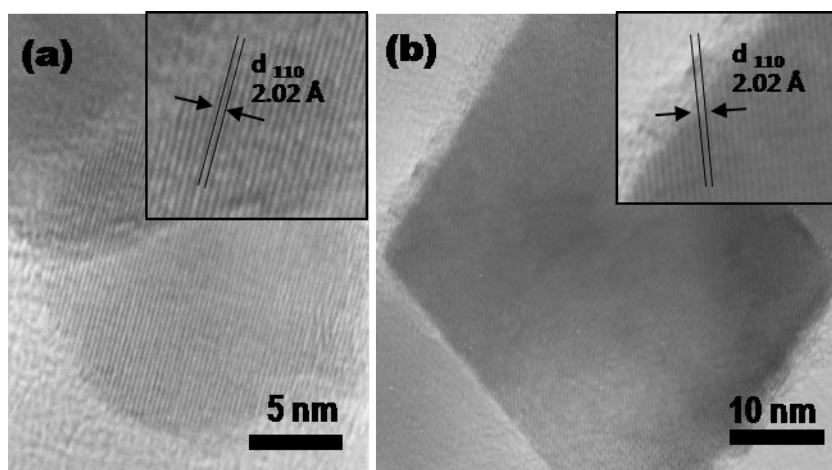


Figure 1.7. HR-TEM image (a and b) of α -Fe nanoparticles annealed with NaCl powder under high vacuum system.

4.4. Decomposition of oleate

The EDX spectrum of Figure 1.8 shows that the atomic ratio of Fe/O is 38.34:61.66 in the obtained Fe_3O_4 nanoparticles. By the ratio of Fe and O in Fe_3O_4 , about 10.54% O on the Fe_3O_4 nanoparticles existed as an organic complex after thermal decomposition in the pyrex tube. Figure 1.9 and Figure 1.10 shows the TGA curve and EPMA spectrum of washed α -Fe nanoparticles. The TGA curve of the annealed α -Fe nanoparticles shows a small weight loss of 0.08% at 250 °C. The further increase at 400 °C shows an increasing weight percentage of 0.6% because of the oxidation of the α -Fe nanoparticles. This indicates that all removable organic materials on the α -Fe nanoparticles were removed at temperatures under 900 °C. This result was in good agreement with that of the EPMA data (Figure 1.10). The EPMA analysis shows that the mol ratio of Fe/O is 90.39:9.60 in the

washed α -Fe nanoparticles and no other elements were found. This means that coated oleate and used NaCl were removed completely.

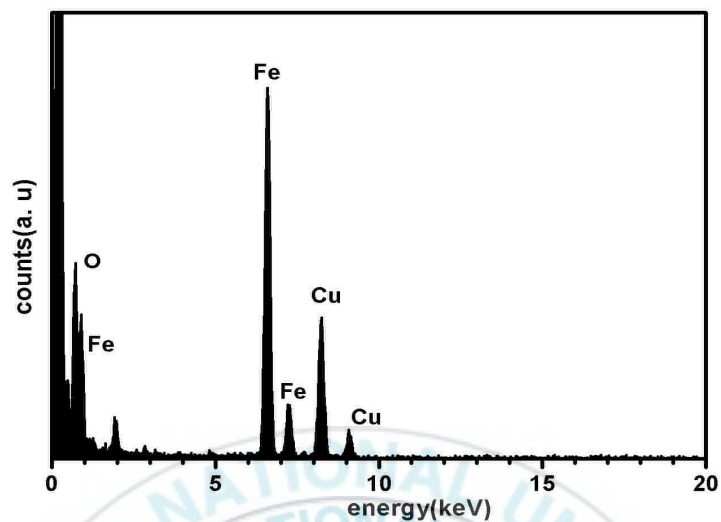


Figure 1.8. EDX spectrum of Fe_3O_4 nanoparticles.

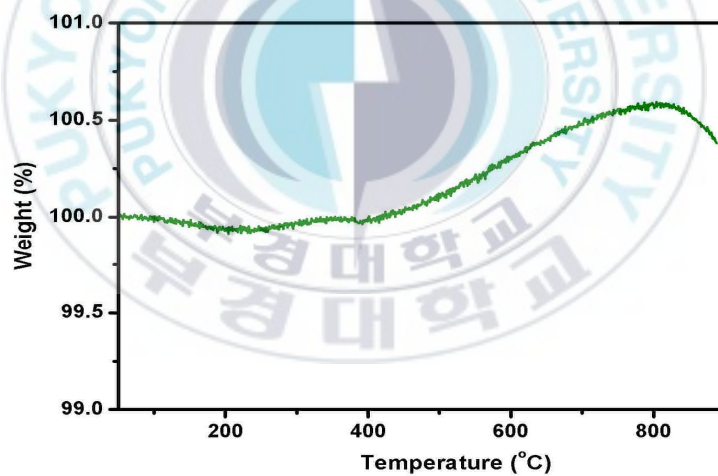


Figure 1.9. TGA curve of α -Fe nanoparticles annealed with NaCl powder under high vacuum system.

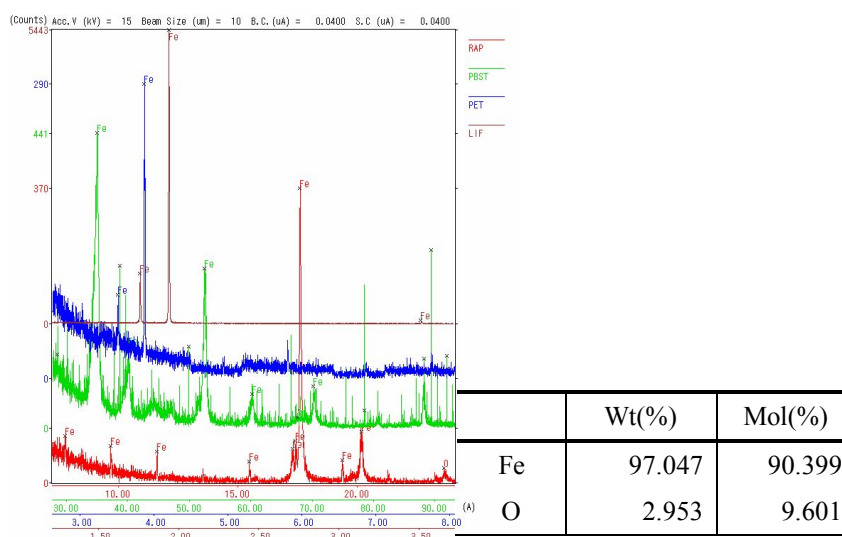


Figure 1.10. EPMA data of α -Fe nanoparticles annealed with NaCl powder under high vacuum system.

4.5. Magnetic property of nanoparticles

Figure 1.11 and Table 1.2 displays the hysteresis loop of obtained α -Fe and Fe_3O_4 nanocrystals by VSM at room temperature. As can be seen in Figure 1.11, when the external magnetic field is applied at 15 kOe, these Fe_3O_4 and α -Fe nanoparticles were not saturated. But, from this measured data, the behavior of the magnetic properties can be confirmed. The saturation magnetization value (M_s) of synthesized Fe_3O_4 nanoparticles is 71.01 emu/g (Figure 1.11, a). When prepared Fe_3O_4 nanoparticles were reduced under a high vacuum of 1.8×10^{-5} torr with NaCl powder, the transformed α -Fe nanoparticles show a saturation magnetization value of 213.00 emu/g (Figure 1.11, b) by removing oleates. This is a higher M_s value than the M_s value of 191.16 emu/g of α -Fe obtained by just the reduction with Ar + H_2 gas

at 800 °C for 3 hrs. The M_s value of the annealed α -Fe nanoparticles is almost equivalent to that of bulk Fe. When the metal nanoparticles were produced by thermal decomposition from the metal-organic complexes, the α -Fe nanoparticles generally show a low magnetic property by the behavior of spin pinning by interactions between the organic surfactant and the surface spins of nanoparticles.¹³ However, after annealing over 800 °C, the particle size and magnetic property were increased due to the particle growth and removal of oleate by the decomposition of organic surfactant.²⁶ When the prepared nanoparticles were annealed under low pressure with NaCl, the magnetic property was increased more. This means that the removal rate of the surfactant coated on the α -Fe nanoparticles is affected more by the magnetic property than the particle size.

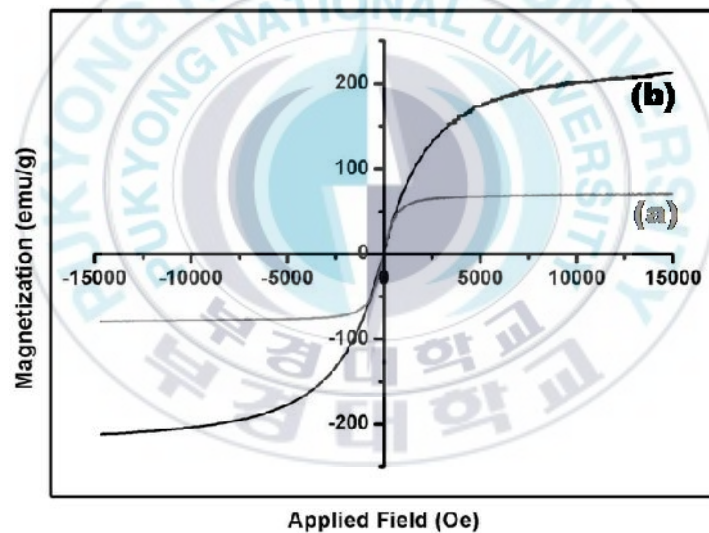


Figure 1.11. VSM curves of prepared nanoparticles: (a) prepared Fe_3O_4 nanoparticles and (b) α -Fe nanoparticles annealed with NaCl powder under high vacuum.

Table 1.2: Magnetic properties of prepared Fe₃O₄ and α -Fe nanoparticles

	M_s (emu/g)	M_r (emu/g)	iH_c (Oe)
Fe ₃ O ₄ (a)	71.01	5.71	51.64
α -Fe (b)	213.00	4.18	57.20

5. Conclusion

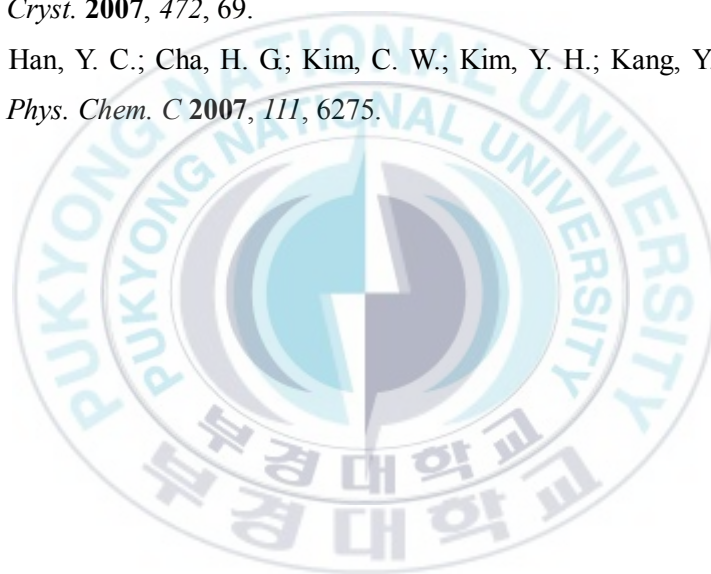
In this experiment, we reported a solventless thermal decomposition method of Fe₃O₄ nanoparticles with NaCl. When the α -Fe nanoparticle was prepared, NaCl powder and a high vacuum system at 10⁻⁵ torr were used. This process is available for the control of morphology and for magnetic properties that were almost equivalent to the M_s values of bulk Fe powder.²⁷

6. References

- (1) Alivisatos, A. P. *Science* **1996**, *271*, 933.
- (2) Lemaire, B. J.; Davidson, P.; Ferre', J.; Jamet, J. P.; Panine, P.; Dozov, I.; Jolivet, J. P. *Phys. Rev. Lett.* **2002**, *88*, 125507.
- (3) Chen, X. Y.; Wang, Z. H.; Wang, X.; Wan, J. X.; Liu, J. W.; Qian, Y. T. *Inorg. Chem.* **2005**, *44*, 951.
- (4) Weddle, K. S.; Aiken, J. D.; Finke, R. G. *J. Am. Chem. Soc.* **1988**, *110*, 5653.
- (5) Zeng, H.; Li, J.; Liu, J. P.; Sun, S. *Nature* **2002**, *420*, 395.
- (6) Cha, H. G.; Kim, Y. H.; Kim, C. W.; Kwon, H. W.; Kang, Y. S. *Curr. Appl. Phys.* **2007**, *7*, 400.
- (7) Rudge, S. R.; Kurtz, T. L.; Vessely, C. R.; Catteral, L. G.; Williamson, D. L. *Biomaterials* **2000**, *21*, 1411.

- (8) Sun, S.; Murray, C. B.; Weller, D.; Folks, L.; Moser, A. *Science* **2000**, *287*, 1989.
- (9) Park, J. N.; An, K.; Hwang, Y.; Park, J.; Noh, H.; Kim, J.; Park, J.; Hwang, N.; Hyeon, T. *Nat. Mater.* **2004**, *3*, 891.
- (10) Wohlfarth, E. P. et al. *Ferromagnetic Materials: A Handbook on the Properties of Magnetically Ordered Substances*; North-Holland: Amsterdam, 1988; p 521.
- (11) Li, X. G.; Takahashi, S.; Watannabe, K.; Kikuchi, Y.; Koishi, M. *Nano Lett.* **2001**, *1*, 475.
- (12) Lee, D. K.; Kim, Y. H.; Zhang, X. L.; Kang, Y. S. *Curr. Appl. Phys.* **2006**, *6*, 786.
- (13) Berkowitz, A. E.; Lahut, J. A.; Jacobs, I. S.; Levinson, L. M. *Phys.Rev. Lett.* **1975**, *34*, 94.
- (14) Cha, H. G.; Kim, Y. H.; Kim, C. W.; Lee, D. K.; Moon, S. D.; Kwon, H. W.; Kang, Y. S. *J. Nanosci. Nanotechnol.* **2006**, *6*, 3412.
- (15) Suslick, K. S.; Fang, M.; Hyeon, T. *J. Am. Chem. Soc.* **1996**, *118*, 11960.
- (16) Lin, H. Y.; Chen, Y. W.; Li, C. *Thermochim. Acta* **2003**, *400*, 61.
- (17) Sayan, P. *Cryst. Res. Technol.* **2004**, *40*, 226.
- (18) Elkins, K.; Li, D.; Poudyal, N.; Nandwana, V.; Chen, Z. K.; Liu, J. *P. J Phys. D: Appl. Phys.* **2005**, *38*, 2360.
- (19) Liu, K. W.; Shen, D. Z.; Zhang, J. Y.; Li, B. S.; Wu, X. J.; Feng, Q. J.; Lu, T. M.; Fan, X. W. *J. Magn. Magn. Mater.* **2006**, *303*, 79.
- (20) Kim, Y. H.; Lee, D. K.; Jo, B. G.; Jeong, J. H.; Kang, Y. S. *Colloids Surf., A* **2005**, *284*, 364.

- (21) Lin, J. H.; Liu, S. F.; Cheng, Q. M.; Qian, X. L.; Yang, L. Q.; Su, M. Z. *J. Alloys Compd.* **1997**, *249*, 237.
- (22) Lee, S. J.; Han, S. W.; Choi, H. J.; Kim, K. J. *Phys. Chem. B* **2003**, *106*, 2892.
- (23) Tadmor, R.; Rosensweig, R. E.; Frey, J.; Klein, J. *Langmuir* **2000**, *16*, 9117.
- (24) Lambrou, P. S.; Efstathiou, A. M. *J. Catal.* **2006**, *240*, 182.
- (25) Zeng, X.; Liu, Y.; Wang, X.; Yin, W.; Wang, L.; Guo, H. *Mater. Chem. Phys.* **2002**, *77*, 209.
- (26) Han, Y. C.; Heo, J. K.; Kim, Y. H.; Kang, Y. S. *Mol. Cryst. Liq. Cryst.* **2007**, *472*, 69.
- (27) Han, Y. C.; Cha, H. G.; Kim, C. W.; Kim, Y. H.; Kang, Y. S. *J. Phys. Chem. C* **2007**, *111*, 6275.



Part II.

Effect of γ -Ray Irradiation on the Permanent Magnets

1. Introduction

Nowadays, radiation techniques are widely applied to processing and studying advanced materials in industrial facilities and medical instruments, such as generating facilities, nuclear fusion reactors, magnetic resonance imaging scanners and computerized tomography. Many research groups have studied the radiation-induced effects on such materials and facilities with ion beams,^{1,2} protons,³ high-energy neutrons⁴ and γ -rays^{5,a}. These studies show that irradiation with γ -rays provides wanted as well as unwanted results and the adverse effects have to be removed. γ -Ray irradiation can cause severe changes to the material properties and is usually unavoidable because of its high permeability. The prediction and control of these changes can be determined by studying the effects of the radiation on materials and facilities.

Permanent magnets are essential for radiation facilities. Many kinds of permanent magnets have been used in industry, communications, transportation and medicine. Some of these applications are in aggressive radiation environments such as high-energy particle accelerators, spectrometers and synchrotron

technology. Nd-Fe-B magnets have a wide field of applications⁷ compared with other permanent magnets such as Al-Ni-Co and Sm-Co. The use of Nd-Fe-B magnets is more practical in radiation-intensive environments, which can cause severe changes in the material properties.^{8,9}

After the first report on the effects of 500 MeV proton irradiation on Nd-Fe-B and Sm-Co magnets in 1985,¹⁰ the decrease of magnetization due to the irradiation has attracted great scientific and technological interest. Results cited in Luna et al.¹¹ and Boockmann et al.¹² have been reported the reduction of magnetism on the ⁶⁰Co irradiation using a hand-held hall probe gauss meter and other analytic device. And Ito et al.¹³ confirmed that the mechanism of demagnetization under the ion beam irradiation is similar to the effects of thermal heating. Moreover, ion-beam-induced flux loss might be attributable to local heating in the magnet, resulting from inelastic collision with the incoming ion beam. However, there have been relatively few studies on the decrease in magnetic properties due to γ -ray irradiation of the rare earth permanent magnets, and the most of these investigations on γ -ray induced damage have been focused on the decreased magnetism of bulk permanent magnets.^{9,14} In this study, the effect of γ -ray irradiation as a condition such as different doses, temperature during the irradiation, surface and size of Nd₂Fe₁₄B magnet was investigated.

2. Theory

Like other strong electromagnetic radiation source, the γ -ray has

enough energy to the ionization of molecules, stripping electrons, and breaking the chemical chain. In case of the magnets, if they are exposed on the γ -ray irradiation, their nature like the magnetism, curie temperature, electronic structure and morphology of surface is also affected. And these properties are significantly depended on the state of magnets and irradiative condition.

As the previously presented studies,¹²⁻¹⁴ if the reason for demagnetization of magnet exposed to the radiation is caused by local heating by γ -ray irradiation, degree of demagnetization is obviously affected by temperature during irradiation time and size of magnets. So, γ -ray irradiation to different sized $\text{Nd}_2\text{Fe}_{14}\text{B}$ magnet was done at low temperature of $-78.5\text{ }^\circ\text{C}$ to confirm the effect of low temperature during the irradiation time to overcome the demagnetization by γ -ray irradiation. Additionally, γ -ray was also irradiated to the fine Nd-Fe-B and Sr-Ferrite magnet powder to confirm changed properties at the fine powder because increased surface area to volume ratio, surface morphology and surface chemistry than their bulk counterparts could be the reasons for advantages in these materials to use the special-purpose such as the high-density magnetic recording media and compacts for high-frequency devices.^{15,16}

3. Experimental

3.1. Materials

The sintered $\text{Nd}_2\text{Fe}_{14}\text{B}$ permanent magnet used for the experiment about the effect of temperature and size on the γ -ray irradiation was a

commercially available magnet referenced N30H purchased from Earth Magnet & Technology and the characteristics are listed in Table 2.1. The size of Nd₂Fe₁₄B samples were approximately 10Φ×15 mm³, 10Φ×10 mm³, 10Φ×5 mm³, 30Φ×10Φ×5 mm³, 10Φ×5Φ×1 mm³, and 5×5×1 mm³. The direction of magnetization was parallel to the cylinder axis and all samples were kept at room temperature for one month to stabilize their magnetic properties.

The SrFe₁₂O₁₉ powders for γ-ray irradiation were purchased from Earth Magnet & Technology referenced P07- H13-SA with an average grain size of 5 μm and used without further treatment. And the fine Nd-Fe-B magnet powder was prepared by ball milling process because the mechanochemical ball milling processing provides a good control over the particle size and produce samples in relatively short times.^{17,18} Pure Nd (99.9%), Fe (99.99%), and B (99.5%) metal to make Nd₁₅Fe₇₇B₈ ingot was purchased from Japan Pure Chemical. Co. and used without further purification. And high purity Ar gas (99.999+%) was used for purging a furnace. To protect from the oxidation, cyclohexane (99.75%) from Junsei Chemical Co. were used.

Table 2.1: Magnetic values of Nd₂Fe₁₄B based magnet(N30H) used in this study.

Materials	Nd ₂ Fe ₁₄ B (0 Mrad)
Br (kGs)	10.8
Hcj (kOe)	17.0
bHc (kOe)	10.5
(BH)max (MGOe)	30

3.2. Preparing the Nd-Fe-B powder

The starting material is the alloy of Nd₁₅Fe₇₇B₈ ingot. Nd₁₅Fe₇₇B₈

alloy ingots were prepared by arc melting Nd, Fe, and B under an argon atmosphere. The prepared ingots wrapped with tantalum foils were homogenized under an argon atmosphere at a temperature of 1070 °C K for 72 hrs. The ingots were crashed to be particle sizes less than 200 mm in diameter by a stamp mill in cyclohexane. And then, the powders were contained in a cylindrical steel port together with 10 mm steel balls and then sealed in an argon-filled glove box. The container was mechanically grinded for 14 hrs by using a high-energy ball mill with a ball to powder weight ratio of 40:1. In order to crystallize the ball milled powders, heat treatment of the powders was done at temperatures of 650 °C for 20 min in furnace at 1.8×10^{-5} torr of vacuum system. The prepared $\text{Nd}_{15}\text{Fe}_{77}\text{B}$ powders were stored in cyclohexane to keep from oxidizing. Figure 2.1 shows the process of Nd-Fe-B particles.

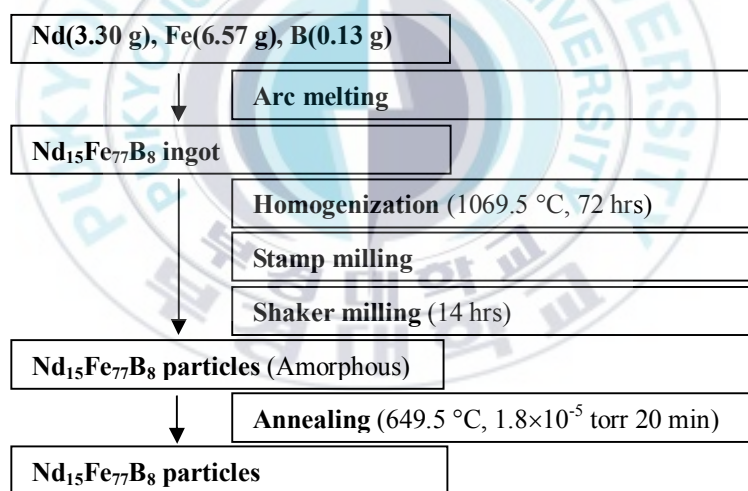


Figure 2.1 The preparing process of Nd-Fe-B particle.

3.3. γ -Ray irradiation

The γ -ray irradiation to the prepared $\text{Nd}_2\text{Fe}_{14}\text{B}$ permanent magnets and ball milled $\text{Nd}_{15}\text{Fe}_{77}\text{B}_8$ and $\text{SrFe}_{12}\text{O}_{19}$ fine powder was carried out in the ^{60}Co γ -ray irradiation room. The irradiation was performed in $\text{Nd}_{15}\text{Fe}_{77}\text{B}_8$ powders stored in cyclohexane to keep from oxidizing and $\text{Nd}_2\text{Fe}_{14}\text{B}$ and $\text{SrFe}_{12}\text{O}_{19}$ permanent magnet at ambient using the ^{60}Co (1.173 MeV) γ -ray irradiation source facility of the Korea Atomic Energy Research Institute (KAERI). The samples were irradiated with γ -ray at room temperature of 26.5 °C and low temperature of -78.5 °C using dry ice. And the irradiation doses were varied from 0 to 100 Mrad and time averaged radiation was 58 hrs.

3.4. Characterization

The magnetic field distributions of the $\text{Nd}_2\text{Fe}_{14}\text{B}$ magnets having the different size as mentioned were measured with a hall-probe¹⁹. The magnetic field of magnets was measured to the same areas before and after γ -ray irradiation. The hall-probe placed in a plastic VSM holder as Figure 2.2 was set to measure the vertical magnetic field of the samples. It was fixed at same position by holder of VSM above the top surface of the magnet. The repeatability of this measuring system was within $\pm 0.01\%$. And the magnetic properties such as saturation magnetization (M_s), coercivity (H_c), remanence (M_r) and maximum energy product ($\text{BH}_{(\text{max})}$) of $\text{Nd}_{15}\text{Fe}_{77}\text{B}_8$ and $\text{SrFe}_{12}\text{O}_{19}$ magnets powder were measured at room temperature with a demagnetization curve by Lake Shore 7300 vibrating sample magnetometer (VSM) with applied field up to 15 kOe. After the powder sample was set with wax to prevent physical rotation of the particles, the magnets were

magnetized with a pulse-magnetizer having a magnetic field of around 10 T. The Curie temperature of magnetic phases were determined by a thermal gravimetric analyzer (TGA) with an applied external magnetic field by magnetic accessory for TMA mode of TGA, which was collected at a heating rate of 10 °C/min with the sample kept under a high purity nitrogen (99.99+%) atmosphere. The weight of whittled Nd₂Fe₁₄B for TMA measurement was 7.2 mg and installed sample was weighted as about 30.4 mg. ESR measurements were carried out using Fourier Transform Electron Spin Resonance Spectrometer (JEOL, JES PX2300JEOL). All of the ESR spectra were recorded at the X-band (9.45 GHz). For careful detection of all the peaks in the ESR spectra of Nd₂Fe₁₄B permanent magnets, the field sweep was employed in the magnetic field of 50-850 mT. ESR measurements in the present study were performed at room temperature (25 °C) and ambient condition. The crystal structure of the prepared powders were investigated using an X-ray powder diffraction (XRD) with a Philips X' pert-MPD System using monochromated a Cu-K_α radiation source ($\lambda = 0.154056$ nm). Scanning electron microscopy (SEM) was also performed to observe the changed surface image of Nd₁₅Fe₇₇B₈ and SrFe₁₂O₁₉ powders by using S-2400 (SEM system HITACHI, Japan) operated at an acceleration voltage of 20 kV.

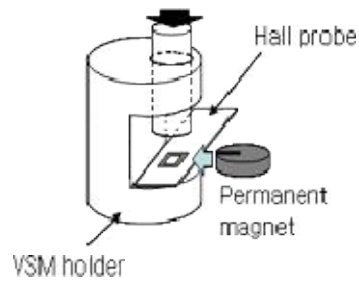


Figure 2.2. Scheme for a Hall probe to measure the magnetic field of samples.

4. Results and Discussion

4.1 Magnetic properties

The dependence of the magnetic field change of sintered $\text{Nd}_2\text{Fe}_{14}\text{B}$ magnets versus irradiation dose of ^{60}Co γ -ray radiation at room temperature and low temperature of $-78.5\text{ }^\circ\text{C}$ was shown in Figure 2.3. As shown in Figure 2.3, sintered $\text{Nd}_2\text{Fe}_{14}\text{B}$ magnets exhibited the different reduction of magnetism by γ -ray irradiation on samples with different sizes of magnets and temperatures. The range of magnetic field change of $\text{Nd}_2\text{Fe}_{14}\text{B}$ magnets exposed to γ -ray irradiation is in the range from $+0.03$ to -2.10% . Their magnetic field change with accumulated dose of 60 Mrad was less than 0.5% except thin $\text{Nd}_2\text{Fe}_{14}\text{B}$ magnets (Figure 2.3 g, h). And, when $\text{Nd}_2\text{Fe}_{14}\text{B}$ magnet was exposed to γ -ray irradiation of 100 Mrad, reduction of magnetic field of most of magnet were gradually occurred. The magnet having thin thickness (Figure 2.3 g, h) has weaker resistance to γ -ray irradiation, and suffers more magnetic field change than other type of magnet. It

notices that the magnetic damage caused by γ -ray irradiation was affected by shape and thickness of magnets. However, when $\text{Nd}_2\text{Fe}_{14}\text{B}$ magnets exposed to γ -ray irradiation at low temperature of $-78.5\text{ }^\circ\text{C}$, these magnets show slightly lower loss of magnetism than that exposed at room temperature. And this resistant phenomenon on the γ -ray irradiation can also confirm for most of magnets having different size.

Room temperature demagnetization curve of the samples of unirradiated and irradiated for heat treated $\text{Nd}_{15}\text{Fe}_{77}\text{B}_8$ powder and $\text{SrFe}_{12}\text{O}_{19}$ powder after γ -irradiation from 25 Mrad to 100 Mrad are shown in Figure 2.4 and 2.5. As you can see in these figures, both the powder showed no signs of saturation at 15 kOe and exhibit very small value of magnetization loss. This present result for low magnetization loss, this is consistent with the previous studies about the γ -ray irradiation to bulk Nd-Fe-B magnet, which bulk Nd-Fe-B permanent magnet at the maximum dose under 100 Mrad showed the low magnetic flux loss of $\pm 0.5\%$.²⁰ Although a gap between each curve is very small, and the observed result about the magnetization for both the powder are less compared to their bulk sample, we confirmed that the irradiated samples show even lesser value of magnetization than that of unirradiated sample as a result of the γ -ray irradiation. Therefore, the both powders irradiated at the temperature of -78.5 K showed less magnetization loss than that at room temperature.

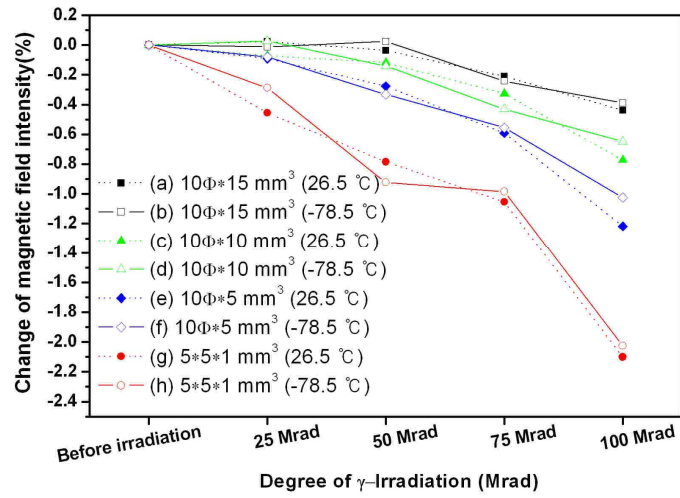


Figure 2.3. The magnetic field change of sintered $\text{Nd}_2\text{Fe}_{14}\text{B}$ magnets having different sizes $10\Phi \times 15 \text{ mm}^3$ (a,b), $10\Phi \times 10 \text{ mm}^3$ (c,d), $10\Phi \times 5 \text{ mm}^3$ (e,f), and $5 \times 5 \times 1 \text{ mm}^3$ (g,h) versus doses of ^{60}Co γ -ray irradiation and temperature.

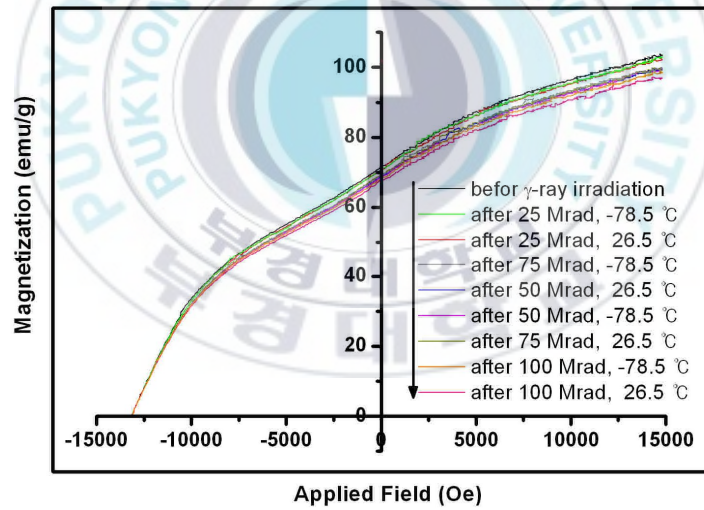


Figure 2.4. VSM curves of ball milled $\text{Nd}_{15}\text{Fe}_{77}\text{B}_8$ powders: as-heat treated and after γ -ray irradiated from 25 Mrad to 100 Mrad at room temperature of $26.5 \text{ }^\circ\text{C}$ and low temperature of $-78.5 \text{ }^\circ\text{C}$.

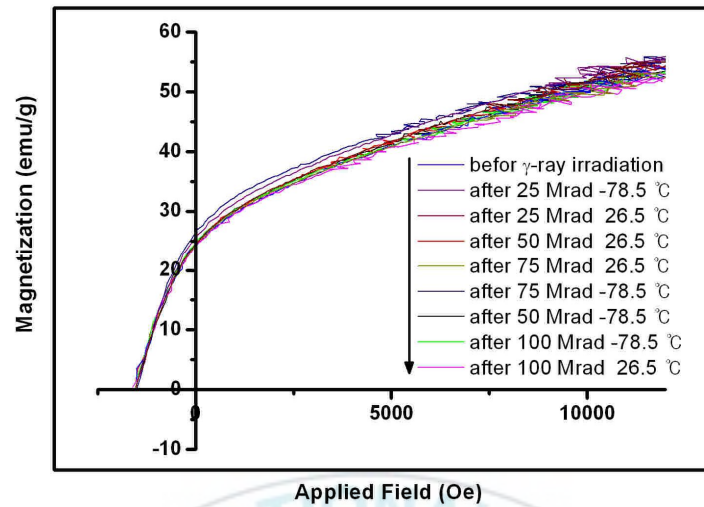


Figure 2.5. VSM curves of $\text{SrFe}_{12}\text{O}_{19}$ powders: as-heat treated and after γ -ray irradiated from 25 Mrad to 100 Mrad at room temperature of $26.5\text{ }^{\circ}\text{C}$ and low temperature of $-78.5\text{ }^{\circ}\text{C}$.

4.2 Ordering energy of domain

Figure 2.6 shows TMA curves for the pristine and γ -ray irradiated $\text{Nd}_2\text{Fe}_{14}\text{B}$ magnets. Figure 2.6 (a) is clear that the value of magnetization decreases with increasing temperature and becomes minimum magnetization at a certain temperature known as T_c of $\text{Nd}_2\text{Fe}_{14}\text{B}$ at $315.21\text{ }^{\circ}\text{C}$. However, the measured result of γ -ray irradiated $\text{Nd}_2\text{Fe}_{14}\text{B}$ magnets at 100 Mrad shows the decreased magnetization value with the increased temperature. And that temperature as the value of T_c is taken at $305.72\text{ }^{\circ}\text{C}$ (Figure 2.6, c). And when $\text{Nd}_2\text{Fe}_{14}\text{B}$ magnets were exposed to γ -ray irradiation at low temperature of $-78.5\text{ }^{\circ}\text{C}$, T_c was measured at $306.43\text{ }^{\circ}\text{C}$ (Figure 2.6, b). The T_c is the magnetic ordering energy of which interactions are

between the local magnetic moments of ions. It can cause the local moments to be ordered or aligned so that there is a net spontaneous magnetization. However, at the high temperature above the T_c , thermal energy suppresses these interactions and then make the disordered state. The decreased T_c for $Nd_2Fe_{14}B$ could be deduced from the fact that the interactions between the local magnetic moments of ions were reduced by γ -ray irradiation. However, as you can see the Figure 2.6 (d), decreasing of T_c value was suppressed about $0.7^\circ C$ when the γ -irradiation was performed at the low temperature. It is the evidence that thermal factor related to the temperature affect to reduction of magnetism by γ -ray irradiation.

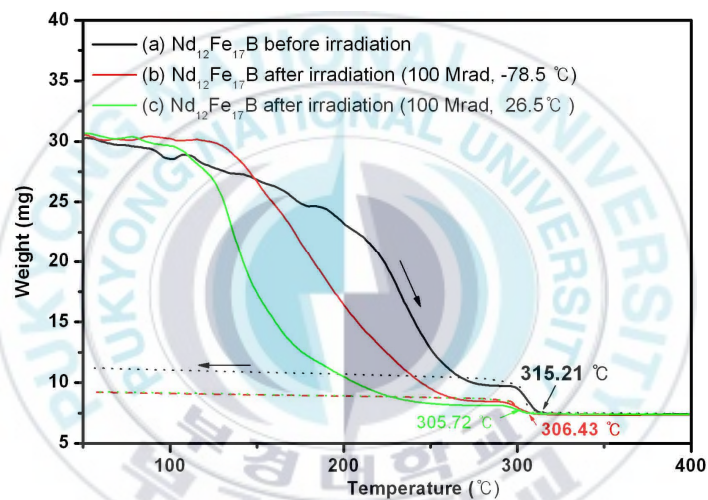


Figure 2.6. The TMA curves of $Nd_2Fe_{14}B$ magnet before (a) and after 100 Mrad of ^{60}Co γ -ray irradiation at low temperature ($-78.5^\circ C$, b) and room temperature ($26.5^\circ C$, c).

4.2 Change of electronic structure

Figure 2.7 shows ESR signals of the $Nd_2Fe_{14}B$ permanent magnets before irradiation and after irradiation at different doses. In ESR

spectra, strong broad singlet peak appears mainly around $g=2.134$ in a fairly constant proportion to the increased doses. It was confirmed that ESR signal at 2.134 is Fe (III) species in a highly symmetric octahedrally coordinated environment^{21,22}. This broad singlet peak causes many chemically similar Fe sites. In neither case the broadness can be due to a single compound such as a macromolecule, with many parts of it clustering round a central Fe atom, because the broadness would require hundreds of parts, which would be impossible because of complicated mixture. Potentially this large peak could also be due to Mn^{+4} (as manganese dioxide) which can have a g -value as high as 2.134 and a similarly broad peak, but the g -value at 2.134 was quite unusual, and we conclude that this identification is quite unlikely. Because the correlation of peaks at $g=4.326$ and $g=2.134$ argues for an identification as Fe. In the result of EDX measurement for $Nd_2Fe_{14}B$ magnet in Figure 2.8, the element of Mn^{+2} was not found. When the dose of γ -ray irradiation of $Nd_2Fe_{14}B$ magnets was increased from 0 Mrad to 100 Mrad, one less broad singlet ESR signal at $g = 4.326$ was observed additionally in the spectra of $Nd_2Fe_{14}B$ magnets. This signal was assigned to Fe (III) in distorted tetrahedral coordination. The ESR intensities of the samples were clearly increased with increasing γ -ray irradiation dose. These results suggest that the amount of Fe (III) ion in Nd-Fe-B magnets increases at $Nd_2Fe_{14}B$ sample with increasing dose of γ -ray irradiation. Figure 2.9 and 2.10 is ESR spectra of the $Nd_2Fe_{14}B$ magnet before and after γ -ray irradiation at 100 Mrad with different microwave power from 0.1 to 140 mW. Figure 2.11 show the variation of the signal intensities of position as P1 peaks in Figure 2.9 and 2.10 at each microwave magnetic field strength, respectively. The

intensity of γ -ray irradiated $\text{Nd}_2\text{Fe}_{14}\text{B}$ (b) leveled off more quickly than the signal of unirradiated one (a). The γ -ray irradiated $\text{Nd}_2\text{Fe}_{14}\text{B}$ signal reflects the shorter relaxation time to present a system relaxes under certain changes in external conditions than the signal of unirradiated one.

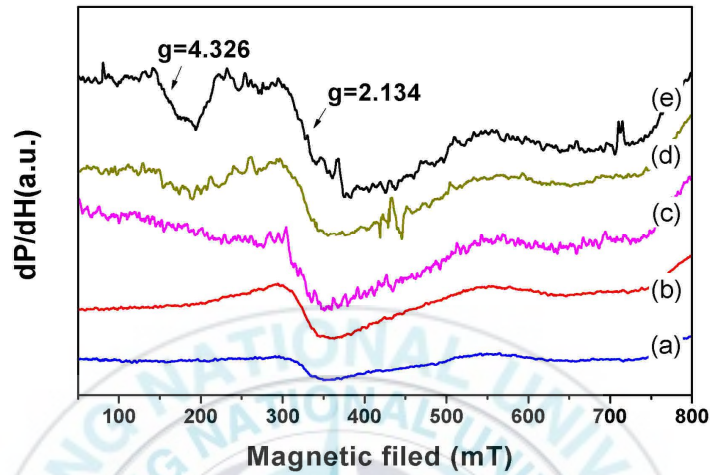
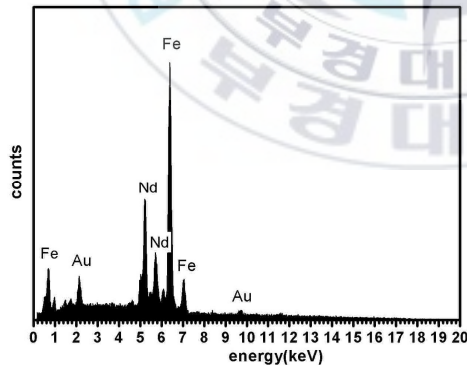


Figure 2.7. The ESR spectra of $\text{Nd}_2\text{Fe}_{14}\text{B}$ magnets before ^{60}Co γ -ray irradiation (a) and after γ -ray irradiation at 25 Mrad (b), 50 Mrad (c), 75 Mrad (d), and 100 Mrad (e).



Element	Weight (%)	Atomic (%)
B	5.24	24.62
O	4.98	15.79
Fe	50.30	45.71
Nd	39.48	13.89

Figure 2.8. The EDX spectrum of $\text{Nd}_2\text{Fe}_{14}\text{B}$ magnets.

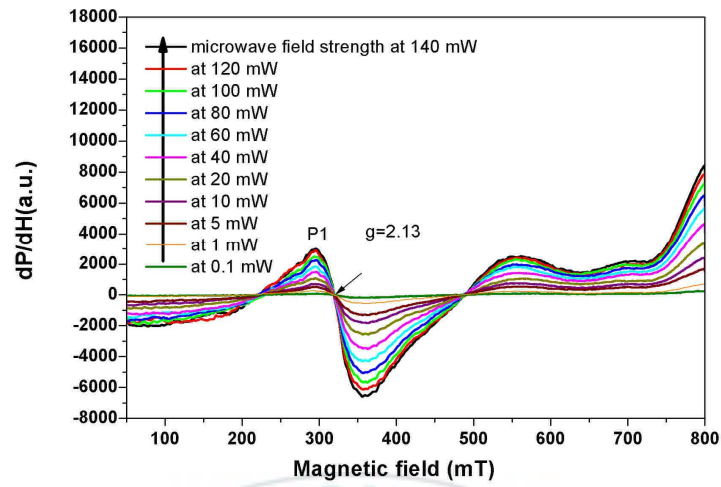


Figure 2.9. ESR spectra of the $\text{Nd}_2\text{Fe}_{14}\text{B}$ magnet before γ -ray irradiation with different microwave power.

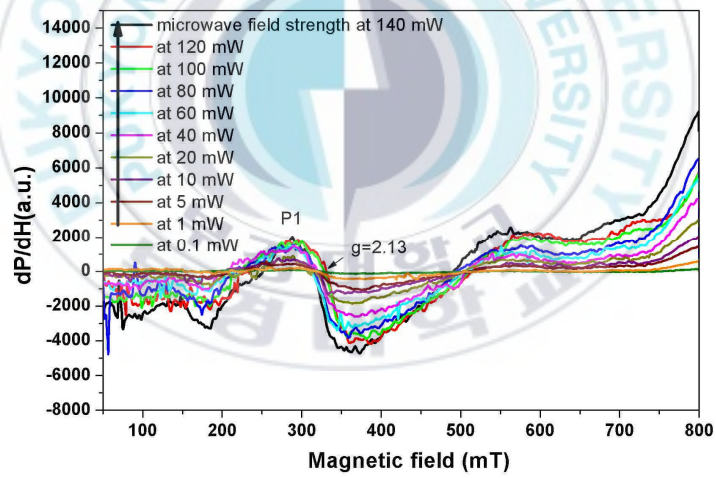


Figure 2.10. ESR spectra with different microwave power of the $\text{Nd}_2\text{Fe}_{14}\text{B}$ magnet after γ -ray irradiation at 100 Mrad.

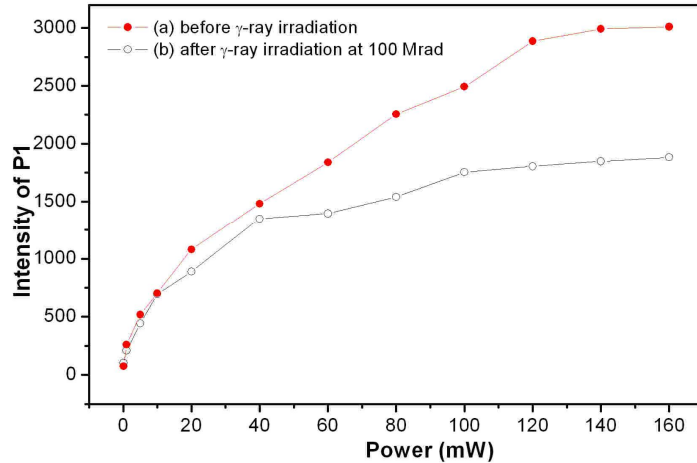


Figure 2.11. Progressive saturation of the $\text{Nd}_2\text{Fe}_{14}\text{B}$ magnet before (a) and after γ -ray irradiation at 100 Mrad (b) by ESR spectra with different microwave powers.

4.4 Crystal structure of Nd-Fe-B and Sr-Ferrite powder

The crystal structure of ball milled $\text{Nd}_{15}\text{Fe}_{77}\text{B}_8$ and $\text{SrFe}_{12}\text{O}_{19}$ powder was analyzed by XRD diffraction. And it is shown in Figure 2.12 and 2.13. Figure 2.12 (a) is the XRD pattern of prepared $\text{Nd}_{15}\text{Fe}_{77}\text{B}_8$ alloy powders which were not exposed to γ -ray irradiation. The XRD pattern of the powders annealed at 1069.5°C shows peaks from α -Fe and $\text{Nd}_2\text{Fe}_{14}\text{B}$, it indicates that the powder consists of their mixture. Although the diffraction peaks of α -Fe are existed in the XRD pattern of the prepared Nd-Fe-B powder, another main peaks are corresponding to tetragonal $\text{Nd}_2\text{Fe}_{14}\text{B}$ (JCPDS card No.86-0273), and these peaks can be indexed to (410), (214), (314), (313), (411), and (619) planes of tetragonal unit cell. The XRD patterns of the $\text{Nd}_{15}\text{Fe}_{77}\text{B}_8$ alloy powders which were exposed to γ -ray irradiation at 25 Mrad and 100 Mrad at room temperature and low temperature were

shown in Figure 2.12 (b) to (e). The peak position in XRD patterns irradiated and unirradiated $\text{Nd}_{15}\text{Fe}_{77}\text{B}_8$ magnets were not remarkably changed at the main peaks after magnets were exposed on γ -ray at 25 Mrad under room temperature and low temperature of $-78.5\text{ }^\circ\text{C}$. But the reduced peak intensity of $\text{Nd}_{15}\text{Fe}_{77}\text{B}_8$ exposed at 100 Mrad at room temperature compared to unirradiated one can be observed and this intensity diminution was reduced when the magnet powder was exposed to the γ -ray irradiation at temperature of $-78.5\text{ }^\circ\text{C}$ compared with the result of room temperature. It means that γ -ray effect at low temperature ($-78.5\text{ }^\circ\text{C}$) to magnetic materials is reduced than at room temperature. Figure 2.13 shows the crystal structure of prepared $\text{SrFe}_{12}\text{O}_{19}$ powders which were exposed to γ -ray irradiation from 0 and 100 Mrad at room temperature and low temperature. All of the peaks were clearly identified with crystal structure of $\text{SrFe}_{12}\text{O}_{19}$ (JCPDS card No.84-1531). In contrast with $\text{Nd}_2\text{Fe}_{14}\text{B}$, XRD pattern of $\text{SrFe}_{12}\text{O}_{19}$ powders does not show the conspicuous change due to γ -ray irradiation.

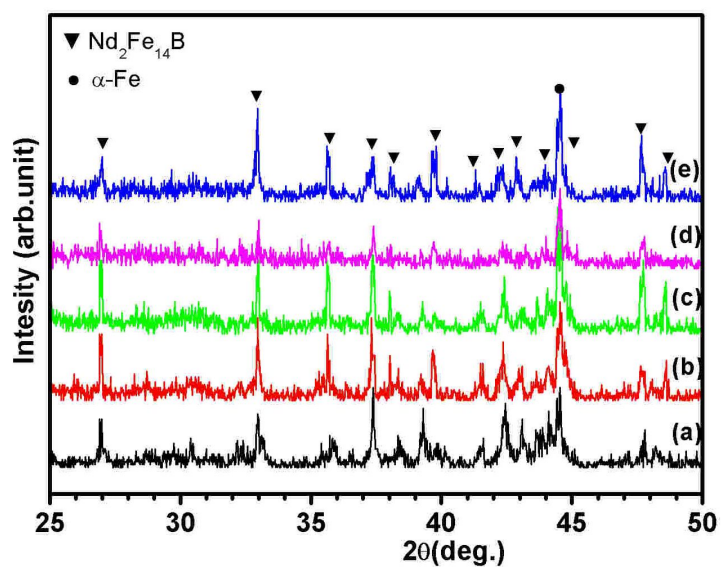


Figure 2.12. XRD pattern of ball milled $\text{Nd}_{15}\text{Fe}_{77}\text{B}_8$ powders: as-heat treated (a), after γ -ray irradiated of 25 Mrad at 26.5 °C (b), 25 Mrad at -78.5 °C (c), 100 Mrad at 26.5 °C (d), 100 Mrad at -78.5 °C (e).

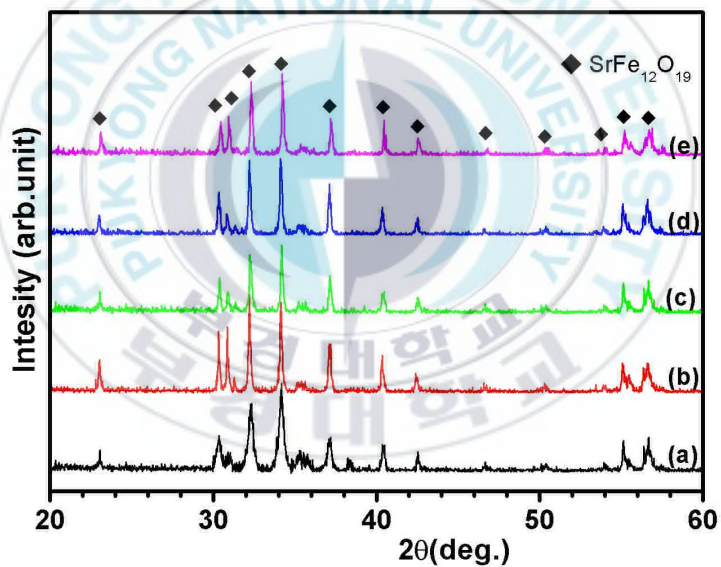


Figure 2.13. XRD pattern of $\text{SrFe}_{12}\text{O}_{19}$ powder: before γ -ray irradiated (a), after γ -ray irradiated of 25 Mrad at 26.5 °C (b), 25 Mrad at -78.5 °C (c), 100 Mrad at 26.5 °C (d), 100 Mrad at -78.5 °C (e).

4.5 Morphology of Nd-Fe-B and Sr-Ferrite powder

Figure 2.14 shows SEM image of ball milled $\text{Nd}_{15}\text{Fe}_{77}\text{B}_8$ powder which was not irradiated with γ -ray (a) and irradiated at 25 Mrad at room temperature (26.5 °C) (b) and low temperature (-78.5 °C) (c), and (d) and (e) are $\text{Nd}_{15}\text{Fe}_{77}\text{B}_8$ powders irradiated at 100 Mrad at room temperature (26.5 °C) and low temperature (-78.5 °C). As you can see in Figure 2.14 (a), the mean size of as-prepared $\text{Nd}_{15}\text{Fe}_{77}\text{B}_8$ powders is 5 μm . Moreover, it shows that the shape of the particles under 1 μm was a spherical and needle shape and over 10 μm was small lump. When γ -ray of 100 Mrad was induced to the prepared $\text{Nd}_{15}\text{Fe}_{77}\text{B}_8$ powder, we confirmed that particles of needle shape were disappeared and most of the edge of small particles was worn down by γ -ray irradiation. The effect of temperature during the γ -ray irradiation has been found between the Figure 2.14 (b) and (c). In case of γ -irradiation at 25 Mrad, the changed surface image and morphology were observed to be lesser compared with case of 100 Mrad but the sensible change of morphology is displayed at 26.5 °C compared with -78.5 °C. The same trend is shown in the case of $\text{SrFe}_{12}\text{O}_{19}$ powders in Figure 2.15. Figure 2.15 shows the SEM images of $\text{SrFe}_{12}\text{O}_{19}$ powders as prepared and after irradiated at 25 Mrad and 100 Mrad. After it was exposed to γ -ray irradiation at 100 Mrad, the changed particle shape of $\text{SrFe}_{12}\text{O}_{19}$ powders as the $\text{Nd}_{15}\text{Fe}_{77}\text{B}_8$ powder was observed between the Figure 2.15 (a) and (d).

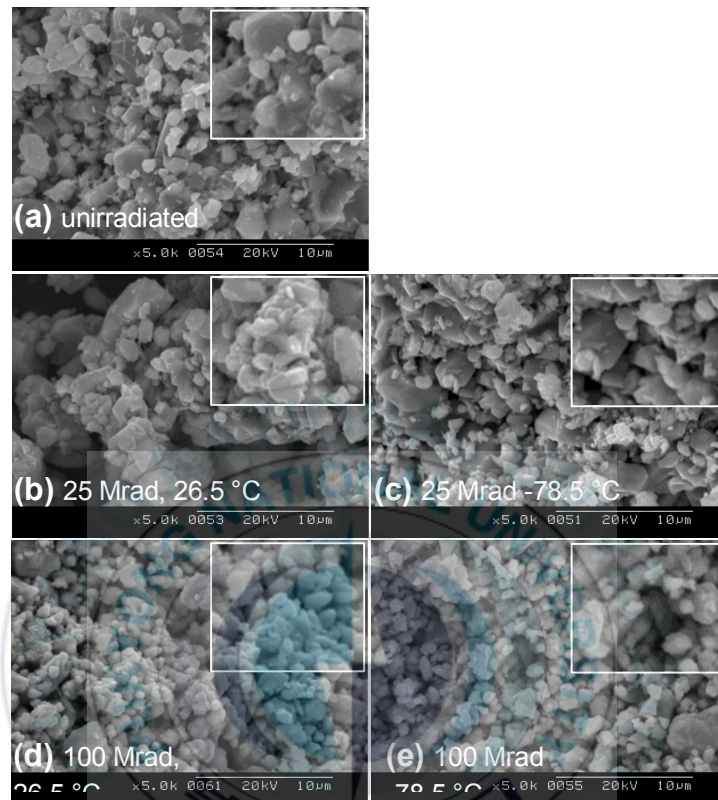


Figure 2.14. SEM images of ball milled $\text{Nd}_{15}\text{Fe}_{77}\text{B}_8$ powders: as-heat treated (a), after γ -ray irradiated of 25 Mrad at 26.5 °C (b), 25 Mrad at -78.5 °C (c), 100 Mrad at 26.5 °C (d), 100 Mrad at -78.5 °C (e).

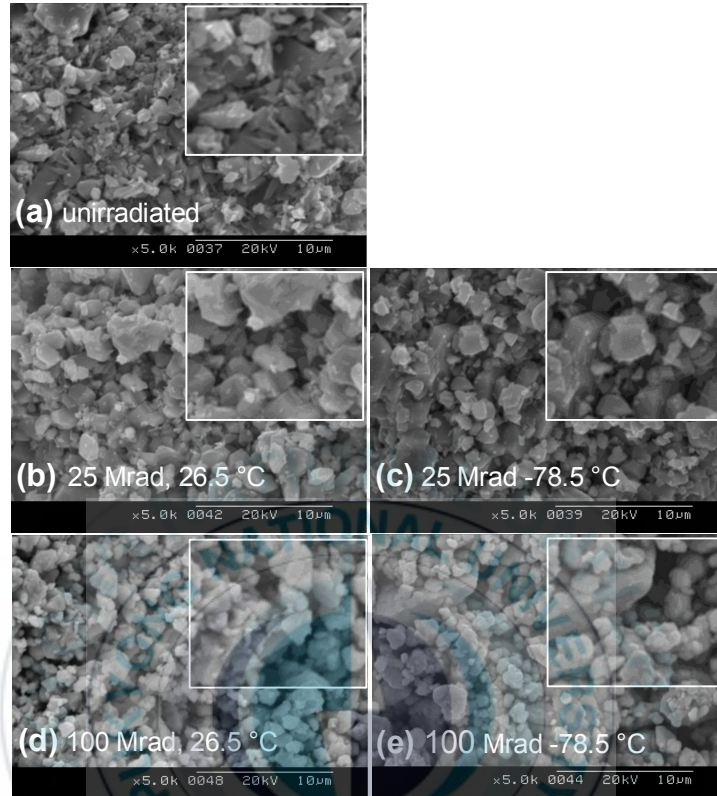


Figure 2.15. SEM images of SrFe₁₂O₁₉: before γ -ray irradiated (a), after γ -ray irradiated of 25 Mrad at 26.5 °C (b), 25 Mrad at -78.5 °C (c), 100 Mrad at 26.5 °C (d), 100 Mrad at -78.5 °C (e).

5. Conclusion

Conclusions from the several previous studies were mostly empirical, and the mechanisms of interaction of radiation with magnetic materials are not fully understood but it is clear that irradiation with neutrons, ionizing radiation or even with γ -rays is able to produce defects and matrix rearrangements to most materials²³. From this study, two major effect of the γ -ray irradiation on the permanent magnet can be confirmed. One effect is the regional thermal heating in the permanent magnet by γ -ray irradiation. And other effect is electronic defect.

In the experiment about effect of γ -ray at the condition of magnet kept lower temperature of $-78.5\text{ }^{\circ}\text{C}$, we can know that the increasing of temperature in local area by exposure to the γ -ray was suppressed and the temperature at the irradiation time is affected to the reduction of magnetism and it can be evidence that regional thermal heating by γ -ray is reason of reduced magnetism as result of Ito et al. and Talvitie et al.^{14,24} Like the neutron beam, γ -ray irradiation also has the enough energy for thermal heating. If the high γ -ray are irradiated into magnetic materials, atoms and electrons can be excited or ionized by inelastic interactions with the γ -ray and, high energy are generated due to secondary electrons and the Compton effect by collisions of γ -ray. Some part of this energy affects to the domain of magnetic material, which may lead to regional temperature increase in a lattice above the Curie point and reduce the magnetism.

Okuda et al. have shown that the reason for the magnetic loss is not

the crystal structural change of the bulk permanent magnets due to irradiation damage²⁵⁻²⁷. However, our results about the crystal structure of Nd₁₅Fe₇₇B₈ powder γ -ray irradiated at 100 Mrad did not agree with that of the previous studies as XRD pattern and SEM image even if the value of magnetization loss is very low. In contrast with bulk permanent magnet, the observed surface of Nd₂Fe₁₄B and SrFe₁₂O₁₉ powder was worn down because of increased surface area to volume ratio, but the XRD spectrum of SrFe₁₂O₁₉ powders appear the unchanged pattern contrary to that of Nd₁₅Fe₇₇B₈ powders and this difference could be due to the accelerated corrosion of Nd₂Fe₁₄B by γ -irradiation. The nature of γ -ray is the electron sources and it accelerates corrosion on surface of alloy powders by the oxidation processes. Unlike the stable SrFe₁₂O₁₉ against oxidation, Nd₂Fe₁₄B magnet alloys show a very low resistance against corrosion by the fast oxidation of the Nd- and B-rich phase located around the grains of the Nd₂Fe₁₄B in various environments²⁸. Moreover, we confirmed that this corrosion by γ -irradiation was suppressed at low temperature of -78.5 °C as the study of C. H. Chen et al.²⁹ about a neutron irradiation on Nd-Fe-B and Sm₂Co₁₇ magnet at temperature of 285.5 °C, that the magnetic flux loss is increased at environment of high temperature. And we could deduce that the effect of γ -ray on the magnetism, micro-crystalline structure and electronic structure of Nd₂Fe₁₄B permanent magnet was critically changed. When Nd₂Fe₁₄B permanent magnet was exposed to γ -ray, their magnetic properties like magnetic field intensity and T_c were changed and their micro-crystal structure and electronic structure were also undergone a change. This result indicates that the electronic defect in Nd₂Fe₁₄B magnets was formed

by γ -ray irradiation, and the effect of formed defect was increased with the dose of γ -ray irradiation. These phenomenon was observed in other influenced environment and other materials.^{30,31}

The Nd-Fe-B permanent magnet is composed with multiple phases such as $\text{Nd}_2\text{Fe}_{14}\text{B}$ (matrix phase), $\text{Nd}_{1+\epsilon}\text{Fe}_4\text{B}_4$ (boron-rich phase), Nd_4Fe (neodymium-rich phase), and other phases in the microstructure generally. These phases allow the high performance of Nd-Fe-B based permanent such as high saturation magnetization and coercivity. Among these phases, $\text{Nd}_{1+\epsilon}\text{Fe}_4\text{B}_4$ and Nd_4Fe phases located around the grain of the $\text{Nd}_2\text{Fe}_{14}\text{B}$ phase to occur at the grain boundaries of matrix phase or at grain junctions are easily collapsed and oxidized by insecure environment. When these phases were placed in unstable environment such as γ -ray, these phases were collapsed and whole grains of $\text{Nd}_2\text{Fe}_{14}\text{B}$ phase were broken off from the structure. As this phenomenon, the γ -ray having high energy and permeability also affected to the susceptible $\text{Nd}_{1+\epsilon}\text{Fe}_4\text{B}_4$ and Nd_4Fe phases in Nd-Fe-B magnet. In other words, at these week phase, defect was made by increasing secondary electron and compton effect which will be elastic collision between ejected γ -ray photon and electron in outer shell of B and Nd atom nuclei.

6. References

- (1) Allens, J.; Anderson S.; Spencer J.; Wolf Z.; Park M.; Boussoufi M.; McClellan, in: *Proceedings of the EPAC 2004, Lucerne, Switzerland*, **2004**, p. 1795.
- (2) Pfluger, J.; Faatz, B.; Tischer, M.; Vielitz, T. *Nucl. Instr. Meth., A* **2003**, *507*, 186.
- (3) Ito, Y.; Yasuda, K.; Ishigami, R.; Hatori, S.; Okada, O.; Ohashi, K.; Tanaka, S. *Nucl. Instr. Meth., B* **2001**, *183*, 322.
- (4) Cost, J. R.; Brown, R. D.; Giorgi, A. L.; Stanley, J. T., *Mater. Res. Soc. Proc.* **1987**, *96*, 321.
- (5) Nakamura, H.; Ukai, M.; Shimoyamac, Y. *Spectrochim. Acta, A* **2006**, *63*, 883.
- (6) Han, Y. C.; Lee, S.; Ahn, B. H.; Oh, S. W.; Kang, Y. S. *Sens. Actuators, A* **2007**, *126*, 266
- (7) Corner W. D., *Phys. Technol.* **1988**, *19*, 158.
- (8) Ito, Y.; Yasuda, K.; Ishigami, R.; Sasase, M.; Hatori, S.; Ohashi, K.; Tanaka, S.; Yamamoto, A., *Nucl. Instr. Meth., B* **2002**, *191*, 530.
- (9) Rao, B. P.; Rao, K. H.; SubbaRao, P. S. V.; Kumar, A. M.; Murthy, Y. L. N.; Asokan, K.; Siva Kumar, V. V.; Kumar, R.; Gajbhiye, N. S.; Caltun, O. F., *Nucl. Instr. and Meth., B* **2006**, *244*, 27.
- (10) Blackmore, E.W., *IEEE Trans. Nucl. Sci.* **1985**, *NS-32*, 3669.
- (11) Boockmann, K.; Liehr, M.; Rodewald, W.; Salzborn, E.; Schlapp, M.; Wall B., *J. Magn. Magn. Mate.* **1991**, *101*, 345.
- (12) Luna; H. B.; Maruyama; X. K.; Colella; N. J.; Hobbs; J. S.;

- Hornady, R. S.; Kulke, B.; Palomar, J. V. *Nucl. Instr. and Meth., A* **1989**, 285, 349.
- (13) Ito; Y.; Yasuda; K.; Ishigami; R.; Ohashi; K.; Tanaka, S. *Nucl. Instr. and Meth., B* **2006**, 245, 176.
- (14) Coey, J. M. D., in *Rare-Earth Iron Permanent Magnets*, Oxford Science Publications, **1996**, p. 99.
- (15) Zhang, L.; Papaefthymiou, G. C.; Ziolo, R. F.; Ying, J.Y., *Nanostruct. Mater.* **1997**, 9, 185.
- (16) Hern/mdez, P.; de Francisco, C.; Mufioz, J. M.; Ifiguez, J.; Tortes, L.; Zazo, M., *J. Magn. Magn. Mater.* **1996**, 123, 157.
- (17) Harada, T.; Kuji T. *J. Alloys Comp.* **1996**, 232, 238.
- (18) Cha, H. G.; Kim, Y. H.; Kim, C. W.; Kwon, H. W.; Kang, Y. S., *J. Phys. Chem. C.* **2007**, 111, 1219.
- (19) Bizena, T.; Asanob, Y.; Harac, T.; Marechala, X.; Seikea, T.; Tanakac, T.; Leed, H. S.; Kimd, D. E.; Chungd, C. W.; Kitamura, H. *Nucl. Instr. Meth. Phys. Res., B* **2003**, 515, 850.
- (20) Gao, R. S., Zhen, L.; Li, G. A.; Xu, C. Y.; Shao, W. Z., *J. Magn. Magn. Mater.* **2006**, 302, 156.
- (21) Szostak, R.; Nair, V.; Thomas, T. L. *J. Chem. Soc. Faraday Trans.* **1987**, 1, 487.
- (22) Kucherov, A. V.; Slikin, A. A, *Zelites* **1988**, 8, 110.
- (23) Devine R. A. B. *Nucl. Instr. Meth. B* **1994**, 91, 378.
- (24) Talvitie M.; Kahkonen O. P.; Makinen S.; Rajainmali H.; Manninen M.; Lindroor V. *J. Magn. Magn. Mater.* **1991**, 102, 323
- (25) Okuda S.; Ohashi K.; Kobayashi N. *Nucl. Instr. Meth. B* **1994**, 94, 227.

- (26) Luna H. B.; Maruyama X. K.; Colella N. J. *Nucl. Instr. Meth. A* **1989**, 285, 349.
- (27) Alderman J.; Job P. K., Puhl J. *Nucl. Instr. Meth. A* **2002**, 481, 9.
- (28) Schultz L.; El-Aziz A. M.; Barkleit G.; Mummert K. *Mater. Sci. Engi. A* **1999**, 267, 307.
- (29) Chen C. H.; Liu J.; Vora P; Higgns A., Liu S. *IEEE Trans. Magn.* **2005**, 41, 3832.
- (30) Kurahashi E.; Yamanaka C.; Nakamura K.; Sasaki S. *Earth plans space* **2002**, 54, e5.
- (31) Nagase T.; Nino A.; Umakoshi Y. *Mater. Sci. Engi. A* **2007**, 449, 1111.



Korean Abstract(국문 요약)

본 연구에서는 열분해법을 이용하여 강자성 α -Fe 나노입자를 합성하였으며, 상온과 저온에서 영구자석에 대한 감마선의 영향에 대해 조사하였다. 순수한 금속 나노입자의 합성에 유용한 열분해법을 통해 얻어진 자성 나노입자는 입자의 표면을 덮고 있는 계면활성제와 그 계면활성제와 입자와의 pinning 현상으로 인해 본래의 자기적 성질을 나타내지 못하며, 일반적인 열처리 과정에서는 나노입자에서 강한 자성을 얻어낼 수가 없다. 본 실험에서는 강자성 나노입자를 제조하기 위해 고온과, 고진공의 환경하에서 NaCl을 사용하여 나노입자를 환원시켰으며 또한 입자의 표면을 덮고 있는 계면활성제를 분해 시켜 본래의 자기적 성질과 동일한 자성을 가지는 α -Fe 나노입자를 합성하였다. 또한 Part 2 에서는 ^{60}Co γ -선이 영구자석에 조사 되었을 때, 영구자석의 자성의 감소와, 감마선 조사시의 온도, T_c , 전기적 구조, 결정구조, 자석표면의 형태의 변화를 확인하였다. 다른 방사선처럼 γ -선도 분자를 이온화 하거나 화학결합을 끊기에 충분한 에너지를 가지고 있으므로 감마선에 노출된 영구자석은 본래의 자성에서 그 성질이 소폭 감소되는 것을 확인 할 수 있다. 감마선에 노출된 Nd-Fe-B 및 Sr-Ferrite계열의 영구자석의 자성 감소 경향을 Gaussmeter, VSM, TMA, XRD, ESR, SEM 등으로 분석하여 자성감소의 원인을 연구하였다.